

Ultralow-Loss Phonon Polaritons in the Isotope-Enriched α -MoO₃

Yongqian Zhao, Jiancui Chen, Mengfei Xue, Runkun Chen, Shangtong Jia, Jianjun Chen, Lihong Bao,* Hong-Jun Gao, and Jianing Chen*



Cite This: *Nano Lett.* 2022, 22, 10208–10215



Read Online

ACCESS |

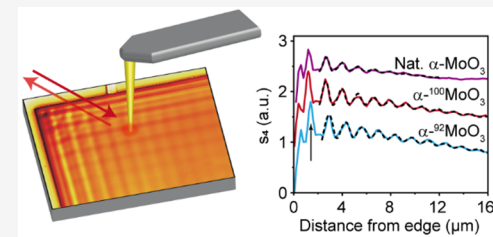
Metrics & More

Article Recommendations

Supporting Information

ABSTRACT: α -MoO₃, a natural van der Waals (vdWs) material, has received wide attention in nano-optics for supporting highly confined anisotropic phonon polaritons (PhPs) from the mid-infrared to the terahertz region, which opens a new route for manipulating light at the nanoscale. However, its optical loss hinders light manipulation with high efficiency. This work demonstrates that the isotope-enriched Mo element enables ultralow-loss PhPs in the α -MoO₃. Raman spectra reveal that the isotope-enriched Mo element in the α -MoO₃ allows different optical phonon frequencies by efficiently altering the Reststrahlen band's dispersion. The Mo isotope-enriched α -MoO₃ significantly reduces the PhPs' optical loss due to efficient optical coherence, which enhances the propagation length revealed by infrared nanoimaging. These findings suggest that the isotope-enriched α -MoO₃ is a new feasible 2D material with an ultralow optical loss for possible high-performance integrated photonics and quantum optics devices.

KEYWORDS: phonon polaritons, hyperbolic materials, near-field imaging, van der Waals materials



Polaritons^{1,2} are an essential concept in modern condensed physics, which are quasiparticles that result from the coupling of photons with polarized charges including the plasmons in graphene,^{3–6} the noble metals,^{7,8} the exciton-polaritons in semiconductors,^{9–12} and the phonon polaritons in polar crystals.^{13–16} The phonon polaritons (PhPs) in hexagonal boron nitride (h-BN)^{17–19} exhibit remarkable advantages in strong field confinement, low loss, and low group velocity and have been widely studied in subdiffraction biosensing, nanoimaging, and superlenses.^{20–24} The hyperbolic phonon polaritons in the h-BN belong to the out-of-plane type; in contrast, in-plane hyperbolic PhPs have recently been discovered in naturally hyperbolic α -MoO₃^{25,26} and α -V₂O₅,²⁷ which provides a new route for the photon manipulation at the nanoscale. Although the optical loss is already much less in the reported PhPs than in the surface plasmon polaritons (SPPs), there is always a need to explore different new methods to reduce optical loss. To reduce the optical loss for achieving more polaritonic applications, researchers have developed several methods to guide and manipulate PhPs. These include (1) variation of the surrounding dielectric environment (It has been demonstrated that the polaritons in different dielectric environments could possess different optical losses.^{18,28–30} However, this method has limited improvement in reducing the PhPs' optical loss.); (2) applying the cryogenic environment (It has been demonstrated that the graphene SPPs could propagate more than 10 μm at low temperatures, much longer than at high temperature.³¹ However, the complicated cryogenic technique limits its practical applications.); and (3) employing isotope enrichment^{32–34} (Compared to natural isotope-disorder materials, it has been demonstrated that the

isotope-enriched materials could significantly improve the thermal conductivity in dielectric solids,^{35–37} and effectively mitigate the PhPs' optical loss in ¹¹B-enriched h-BN.³²

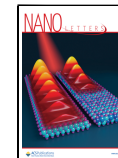
Although the isotope enrichment in the h-BN has achieved long propagation length by effectively reducing the optical loss, h-BN cannot support in-plane hyperbolic polaritons, which hinders its applications in nanophotonics devices. Unlike h-BN, the α -MoO₃ is a natural biaxial vdWs material, supporting in-plane anisotropic PhPs. In-plane anisotropic propagation offers directional control of light,^{25,38} photonic magic angles,¹⁵ and topological polaritons³⁹ at the nanoscale and could be steered in more ways, such as edge-orientation,⁴⁰ which has potential applications in sensing, imaging, and quantum nanophotonics. It is known that ¹⁶O is naturally 99.7% abundant for the α -MoO₃, which is relatively pure. However, the Mo element has seven different stable isotopes ⁹²Mo, ⁹⁴Mo, ⁹⁵Mo, ⁹⁶Mo, ⁹⁷Mo, ⁹⁸Mo, and ¹⁰⁰Mo. Each naturally distributes in a range of 9–24%. These seven Mo isotopes take approximately the same proportion, leading to a substantial optical loss in a natural α -MoO₃.

In this work, we synthesized the high-quality isotope-enriched MoO₃ for the first time with ¹⁰⁰Mo and ⁹²Mo by a physical vapor deposition method. We showed that the

Received: September 23, 2022

Revised: November 2, 2022

Published: November 7, 2022



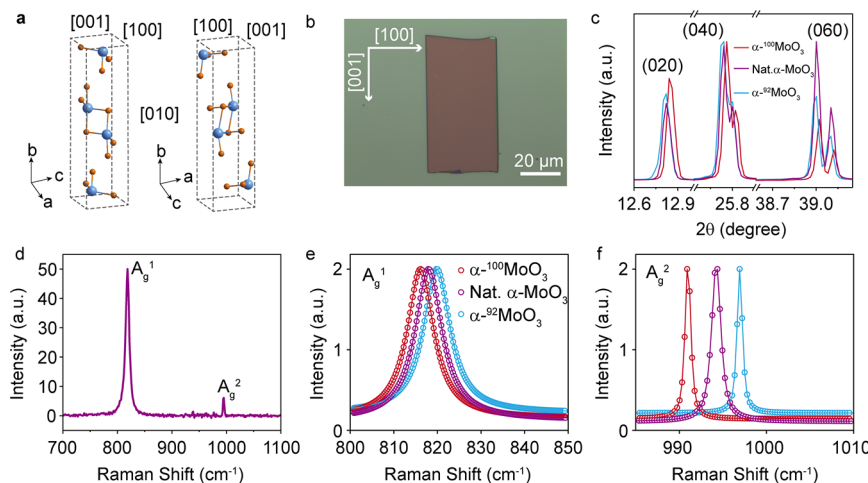


Figure 1. Structural characterizations of natural and isotope-enriched α -MoO₃. (a) Schematic of the crystalline structure of layered α -MoO₃ viewed from [100] and [001] directions. Blue and orange balls represent molybdenum and oxygen atoms, respectively. (b) Optical image of natural α -MoO₃ flakes. The marked arrows indicate [100] and [001] directions of α -MoO₃. The scale bar is 20 μm . (c) XRD patterns of natural α -MoO₃, α -¹⁰⁰MoO₃, and α -⁹²MoO₃. (d) Raman spectra of natural α -MoO₃ flakes. (e, f) Comparison of A_g^1 and A_g^2 Raman mode of natural α -MoO₃, α -¹⁰⁰MoO₃, and α -⁹²MoO₃. The experimental data (hollow circle) were fitted with Voigt profiles (solid lines).

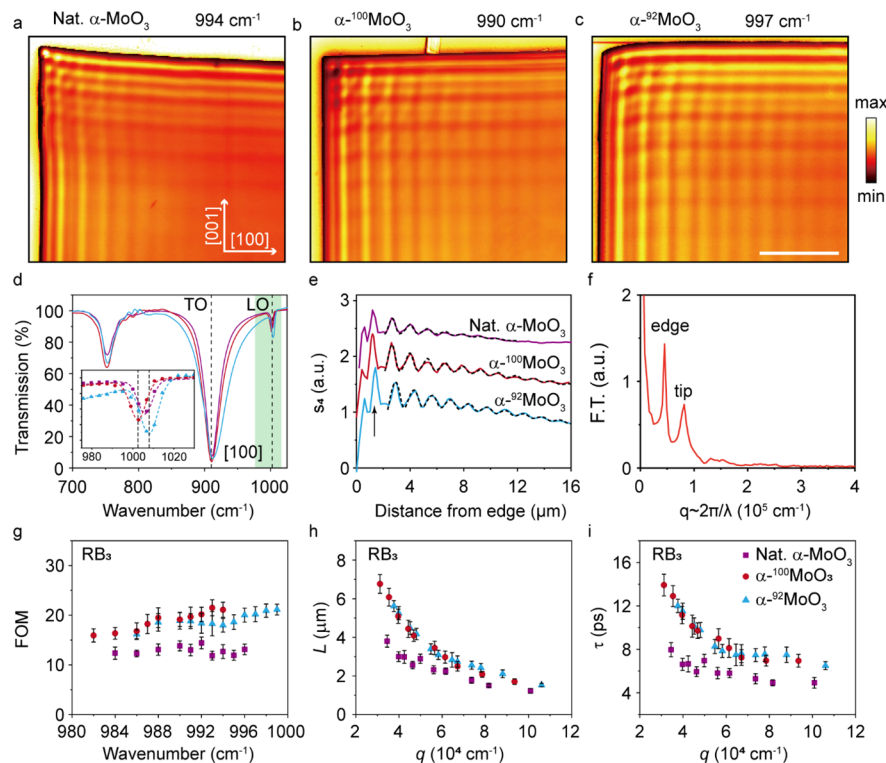


Figure 2. Near-field imaging and PhPs loss of the different α -MoO₃ flakes. (a–c) Experimental near-field amplitude (s_4) images in RB₃ collected from the natural α -MoO₃ at $\omega = 994 \text{ cm}^{-1}$ (panel a), α -¹⁰⁰MoO₃ at $\omega = 990 \text{ cm}^{-1}$ (panel b), α -⁹²MoO₃ at $\omega = 997 \text{ cm}^{-1}$ (panel c). The thicknesses of the α -MoO₃ flakes are about 240 nm, and the scale bar is 5 μm . (d) Micro-FTIR transmission spectra of three different α -MoO₃ with incident polarization parallel to [100] direction. The black dashed lines indicate the range of RB₂ and RB₃ of α -MoO₃. The inset is an enlarged view of the shaded area, the solid dots represent experimental data, and the dashed lines fit the data points using a Gaussian function. The positions of LO phonon for α -¹⁰⁰MoO₃ and α -⁹²MoO₃ are marked by the black dashed line at 1002.5 and 1008 cm^{-1} , respectively. (e) Solid lines in different colors represent the line profiles along the [100] direction extracted from panels a–c. The black dashed lines denote the fitted curves. (f) Fourier transform of the line profiles of natural α -MoO₃ in panel e. (g) FOM of the PhPs in the different α -MoO₃ flakes as a function of illuminating frequencies. (h, i) Propagation lengths and lifetimes of PhPs for different α -MoO₃ flakes in RB₃ as a function of the wave vector. The error bars in panels g–i denote the statistical standard deviations of the FOM, L , and τ and are calculated by the least-squares method.

isotope-enriched α -MoO₃ supports ultralow-loss PhPs at room temperature with a highly improved lifetime of 13.9 ps. Raman spectra exhibit a narrower peak of the longitudinal optical phonon (A_g^2) in the isotope-enriched α -MoO₃, suggesting the

high crystal quality of the synthesized isotope-enriched α -MoO₃. As a new degree of freedom, control over the atomic mass of the Mo element could effectively tune the Reststrahlen band (RB) of the PhPs in the α -MoO₃. Our results

demonstrate that the Mo element isotope-enriched α -MoO₃ effectively reduces the PhPs loss in the α -MoO₃ crystals, which is a potentially realistic candidate for the fabrication of the ultralow-loss polaritonic devices in the future.

As shown in Figure 1a, α -MoO₃ crystal possesses a P_{bmm} space group with lattice parameters of $a = 3.97 \text{ \AA}$, $b = 13.86 \text{ \AA}$, and $c = 3.71 \text{ \AA}$. The α -MoO₃ crystal is a layered material with a strong intralayer chemical bond and weak interlayer vdWs combination and thus is easily mechanically exfoliated. Each layer in the orthorhombic α -MoO₃ crystal is formed by distorted MoO₆ octahedra with multiple nonequivalent Mo—O bonds, and these polar bonds result in the α -MoO₃ optically anisotropic. Generally, α -MoO₃ has three RBs in the mid-infrared range: RB₁ ($545\text{--}851 \text{ cm}^{-1}$), RB₂ ($820\text{--}972 \text{ cm}^{-1}$), and RB₃ ($958\text{--}1010 \text{ cm}^{-1}$). RB is designated as the spectral band ranging from the transverse optical to longitudinal optical phonon frequency along with specific crystal orientation. In each RB, the real part of the permittivity has opposite signs along one axis compared to the other two axes,³⁸ thus enabling α -MoO₃ to support the propagating PhPs.

High-quality α -¹⁰⁰MoO₃ and α -⁹²MoO₃ crystals were synthesized by physical vapor deposition using high pure α -MoO₃ powder with isotope enrichment (⁹²Mo = 99.9% and ¹⁰⁰Mo = 99.0% as precursors). The α -MoO₃ flakes were obtained by mechanically exfoliating the as-grown α -MoO₃ crystal onto the Si substrate. More experimental details can be found in the Methods section. As shown in Figure 1b, the optical image shows the mechanical-exfoliated α -MoO₃ flake with a rectangular shape, intuitively indicating the anisotropic structure of α -MoO₃ crystal. Three prominent XRD peaks (Figure 1c) are assigned to (020), (040), and (060) planes, respectively, clearly indicating the high crystal quality of the as-fabricated α -MoO₃ flakes. However, compared to natural α -MoO₃ crystal, these diffraction peaks slightly blueshift (redshift) for α -⁹²MoO₃ (α -¹⁰⁰MoO₃), indicating that the lattice constants increase (decrease) for α -⁹²MoO₃ (α -¹⁰⁰MoO₃). The above results reveal that the high-quality α -⁹²MoO₃ and α -¹⁰⁰MoO₃ crystals were successfully fabricated, paving the way for subsequent low-loss PhPs realization.

The large anisotropy of the structure leads to sizable optical anisotropy.⁴¹ Figure 1d shows the typical Raman spectra of natural α -MoO₃ flakes excited by $\lambda = 632.8 \text{ nm}$ He–Ne laser. The natural α -MoO₃ presents two Raman modes, in-plane A_g¹ mode at 818.0 cm^{-1} and out-of-plane A_g² mode at 994.2 cm^{-1} , which vibrate along [100] and [010] directions and relate to RB₂ and RB₃, respectively. Furthermore, Raman spectra in Figure 1e and f show that the isotope-enriched α -MoO₃ exhibits significant frequency shifts in A_g¹ and A_g² modes. The A_g¹ and A_g² modes redshifts 1.9 and 3.2 cm^{-1} for the α -¹⁰⁰MoO₃ and blueshifts 1.8 and 2.7 cm^{-1} for the α -⁹²MoO₃ compared to the natural α -MoO₃. This clearly shows that isotope enrichment is an effective method to tune phonon frequency. Additionally, Figure 1f shows that the full-width at half-maximum (fwhm) of A_g² phonon is remarkably reduced to 0.8 cm^{-1} both for α -¹⁰⁰MoO₃ and α -⁹²MoO₃ compared with the 1.3 cm^{-1} of natural α -MoO₃, indicating a considerable increase in phonon lifetime of the isotope-enriched α -MoO₃. The Raman spectra suggest that our synthesized α -MoO₃ crystals are of high quality, which is credible for the subsequent examination of the efficiency of their PhPs.

Phonon lifetime in the α -MoO₃ is a sound signature for evaluating the propagation property of the PhPs. Due to higher coherence, an increased phonon lifetime corresponds to the

decreased optical loss and longer propagation length of the PhPs. We mapped the propagating PhPs on different α -MoO₃ flakes in the mid-infrared regime by scattering scanning near-field optical microscopy (s-SNOM, details in Methods).

Figure 2a–c show the near-field amplitude images of the propagating PhPs in RB₃ in the natural and isotope-enriched α -MoO₃ with similar thickness around 240 nm (more characterization information in Figures S1–S4). The incident light is always adjusted perpendicular to the [001] direction of α -MoO₃ flakes. The fringes parallel to the edges are the near-field optical amplitude signals, representing the propagating PhPs launched by the probe tip and the α -MoO₃ edge. The two mutually perpendicular edges present apparent PhPs fringes parallel to the edges. To achieve similar PhPs wavelength λ_{PhPs} in the ⁹²Mo-enriched and ¹⁰⁰Mo-enriched α -MoO₃ flakes as compared to natural α -MoO₃, the frequency of incident light redshifts 4 cm^{-1} for α -¹⁰⁰MoO₃ and blueshifts 3 cm^{-1} for α -⁹²MoO₃. Figure 2d shows the micro-FTIR transmission spectra of three different α -MoO₃ with incident polarization parallel to [100] direction of α -MoO₃, and α -MoO₃ exhibits obvious absorption peaks around 500, 820, and 1006 cm^{-1} . The inset shows an enlarged view of the longitudinal optical (LO) phonons associated with RB₃, and the peak positions of the LO phonons are clearly separated: the LO phonons of α -¹⁰⁰MoO₃ and α -⁹²MoO₃ are at 1002.5 and 1008 cm^{-1} , respectively. The infrared and Raman phonon frequency (discussed in Figure 1f) changes imply a redshift and a blueshift for α -¹⁰⁰MoO₃ and α -⁹²MoO₃ in RB₃, respectively, compared to the natural α -MoO₃.

Figure 2e shows several line profiles of the PhPs along the [100] direction extracted from Figure 2a–c. The PhPs propagate 7 cycles of perceptible oscillations in the natural α -MoO₃, and 11 cycles of large-amplitude oscillations in the isotope-enriched α -MoO₃, suggesting longer propagation length and lower loss in the isotope-enriched α -MoO₃. As indicated by the black arrow, the amplitude of the first oscillation line profiles for the isotope-enriched α -MoO₃ is significantly higher than that of the natural α -MoO₃, implying higher conversion efficiency from free-space light to PhPs and higher coherence.

In nature, seven stable Mo elements distribute randomly in α -MoO₃. Accordingly, phonons are scattered by these different Mo elements, resulting in a short phonon lifetime and significant optical loss. After replacing with monoisotopic ⁹²Mo and ¹⁰⁰Mo in α -⁹²MoO₃ and α -¹⁰⁰MoO₃, random phonon scatterings are significantly suppressed due to optical coherence enhancement of the PhPs. The longer propagation length of the PhPs in the isotope-enriched α -MoO₃ is a direct indication of the reduced random phonon scattering, which suggests the significant potential of the isotope-enriched α -MoO₃ in promoting the PhP-related applications such as sensing and enhanced spectroscopy.

Near-field optical images directly show that isotope enrichment plays a significant role in reducing the PhPs loss. To explore the impact of the isotope enrichment on the PhPs in detail, we made a quantitative comparison in Figure 2g–i. The following equation⁴² describes the decay in the PhPs propagation:

$$\begin{aligned} E_{\text{total}} &= Ae^{-\alpha qx} \sin(qx + \varphi) + Cx + D \\ (A > 0, D > 0, C < 0, \varphi \in [-\pi, \pi], \alpha \in [0, 1]) \end{aligned} \quad (1)$$

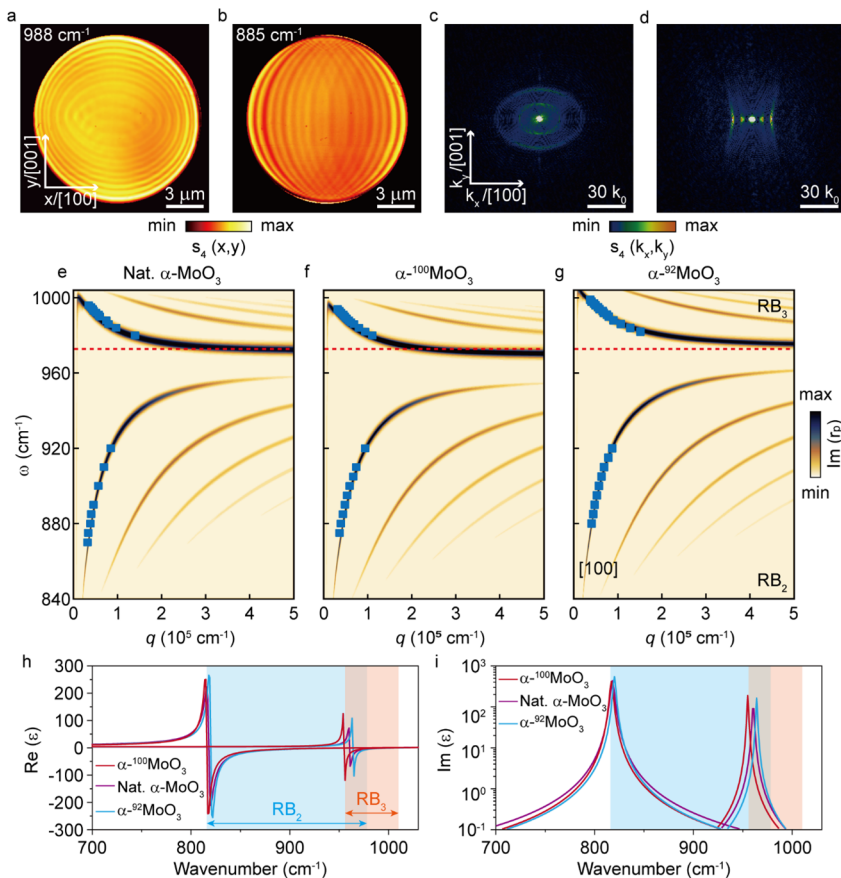


Figure 3. In-plane elliptical hyperbolic PhPs and dispersion of PhPs in the different Mo element isotope-enriched α -MoO₃ flakes. (a, b) Near-field images of the α -⁹²MoO₃ disk with a thickness of 200 nm and diameter of 12 μm at the excitation frequency of 988 and 885 cm^{-1} , respectively. The arrows indicate the crystallographic direction of the α -MoO₃ disk. (c, d) Fourier transform of the near-field images in panels a and b, respectively. The scale bar is $30 k_0$, and k_0 is the momentum of light in free space. (e–g) Dispersion relation of PhPs along [100] direction of a 240 nm-thick natural α -MoO₃, α -¹⁰⁰MoO₃, and α -⁹²MoO₃ flakes on top of the Si substrates. The blue squares represent the experimental data extracted from monochromatic imaging. The false color shows the imaginary part of the Fresnel reflection coefficient. The red dashed line indicates the lower edge of the RB₃ of the natural α -MoO₃. (h, i) Calculated real and imaginary part of the dielectric function on three different isotope-enriched α -MoO₃. The shaded areas indicate the Reststrahlen bands (RB₂ and RB₃).

The first term describes the edge-launched PhPs considered plane waves,⁴³ and the linear function term describes the near-field signal drop away from the edge.⁴⁴ Here, $q_p = q + ik$ represents the complex wave vector, and q and k denote the real and imaginary parts of q_p , respectively. $\alpha = k/q$ denotes the propagation damping. The figure of merit (FOM) is defined as q/k , which characterizes the optical loss feature of the PhPs. Figure 2f shows the Fourier transform (FT) result of the line profiles, and the two peaks indicate the wave vectors of edge-launched and tip-launched PhPs, suggesting two types of excitations in the obtained near-field amplitude images. The peak referring to edge-launched PhPs is significantly higher than the tip-launched PhPs, indicating that edge-launched PhPs are dominant. Therefore, we only consider the edge-launched PhPs in our fitting procedure (see Figure S7).

As shown in Figure 2e, the fitted curves (dashed lines) match the experimental curve well, ensuring the reliability of the calculation of the FOM, the propagation length, and the lifetime. Figure 2g shows that the FOM of the PhPs in RB₃ rises with increasing excitation frequency. The FOMs of the α -⁹²MoO₃ and the α -¹⁰⁰MoO₃ are significantly superior to the natural α -MoO₃ by 1.5-times from 984 to 996 cm^{-1} . Nanostructures, whose geometries are optically optimized, offer a high FOM such as the resonant nanocavities.^{45,46} We

anticipate that optically resonant nanostructures made of isotopically pure polaritonic materials would significantly promote the polaritonic FOM to an unprecedented level.

Propagation length L and lifetime τ are essential parameters for assessing the PhPs loss. Here, we define $L = 1/k$ and $\tau = L/v_g$ of which $v_g = dk/dw$ is the group velocity attainable from the first derivative of the experimental dispersion relations (Figure S6). Figure 2h and i show the L and τ increase as the q decreases, revealing much less PhPs loss at smaller wave vectors. It is worth noting that the L and τ of the α -¹⁰⁰MoO₃ and α -⁹²MoO₃ significantly increase by more than 50% over the natural α -MoO₃ in the entire wave vector range. Remarkably, compared to the propagation length of 2.79 μm and lifetime of 8 ps reported earlier,²⁵ the L and τ of the α -¹⁰⁰MoO₃ rise to 6.76 μm and 13.9 ps, respectively (Figure S9). Such a substantial reduction in optical loss of the PhPs is in good agreement with the decrease in the fwhm of the A_g² phonon modes, suggesting significant potential in promoting PhP-related applications.

To experimentally verify the anisotropic response of the PhPs in the α -MoO₃ flakes, we performed infrared nano-imaging on the α -⁹²MoO₃ disk with a diameter of 12 μm fabricated by a focused ion beam. As presented in Figure 3a and b, the near-field images show elliptical patterns at $\omega = 988$

cm^{-1} in RB_3 , and almond patterns with the opening direction along [100] direction at $\omega = 885 \text{ cm}^{-1}$ in RB_2 . Furthermore, we applied the FT analysis to the patterns in Figure 3a and b and obtained the isofrequency contours in the wave vector space, as shown in Figure 3c and d (Figure S10). The results show that the isofrequency contours present elliptical and hyperbolic shapes, confirming that $\alpha\text{-MoO}_3$ inherently possesses in-plane elliptical dispersion in RB_3 and in-plane hyperbolic dispersion in RB_2 , respectively.

To understand the PhPs, we analyzed the dispersion relation by extracting the λ_{PhPs} from the near-field PhPs line profiles in RB_2 and RB_3 (Figures 3e–g and S11). The in-plane wave vector $q = 2\pi/\lambda_{\text{PhPs}}$ is derived from FT analysis of each line profile, and then we obtained the dispersion relation $w = f(q)$ from the experiments and calculation. The blue dots in Figure 3e–g represent the experimental data extracted from spatial plots. Furthermore, we theoretically calculated the complex reflectivity of the PhPs shown as a false-color plot (see Supporting Information S9) by the Fresnel equations:

$$r_p = \frac{r_a + r_s e^{i2k_2^b d}}{1 + r_d r_s e^{i2k_2^b d}} \quad (2)$$

where the parameters r_a and r_s refer to the reflectivity at the air/ $\alpha\text{-MoO}_3$ and the $\alpha\text{-MoO}_3/\text{Si}$ interfaces, respectively; k_2^b represents the momentum component of the electromagnetic wave propagating along the [100] direction of the $\alpha\text{-MoO}_3$; and d denotes the thickness of the $\alpha\text{-MoO}_3$.

As shown in Figure 3e–g, the dark stripes represent the allowed optical modes of different orders. The fundamental mode with the smallest q in an individual RB corresponds to the principal branch. The PhPs exhibit different dispersion relations in RB_3 ($958\text{--}1010 \text{ cm}^{-1}$) and RB_2 ($820\text{--}972 \text{ cm}^{-1}$). Specifically, the PhPs could propagate along both [100] and [001] directions in the RB_3 , and the q value becomes smaller with increasing ω . In contrast, the PhPs could propagate only along [100] direction in RB_2 (Figure S11), and the q value increases as ω increases. The above results further show the distinct PhPs propagation properties in two RBs of $\alpha\text{-MoO}_3$. All the calculated principal branches (dark stripes) in Figure 3e–g are in good agreement with the experimental data. However, as indicated by the red dashed lines in Figure 3e and g, the darkest stripes deviate significantly from the red dashed lines, indicating an appreciable RB_3 shift in the isotope-enriched $\alpha\text{-MoO}_3$ compared with the natural $\alpha\text{-MoO}_3$. The dielectric function in Figure 3h and i displays the RB's difference on the different $\alpha\text{-MoO}_3$. The RB_3 redshifts 4 cm^{-1} for $\alpha\text{-}^{100}\text{MoO}_3$ and blueshifts 3 cm^{-1} for $\alpha\text{-}^{92}\text{MoO}_3$ compared to the natural $\alpha\text{-MoO}_3$. The shifts of the RB_3 are consistent with the shifts of the A_g^2 phonon in Figure 1f, indicating that isotope enrichment enables varying RB effectively.

In conclusion, we have synthesized high-quality isotope-enriched $\alpha\text{-MoO}_3$ crystals through a physical vapor deposition method. By near-field infrared imaging, we showed that isotope-enriched $\alpha\text{-MoO}_3$ supports ultralow-loss of the PhPs, in contrast to the natural $\alpha\text{-MoO}_3$. The apparent shifts of the PhPs' Reststrahlen band coincide with the mass variations of the Mo element. The isotope enrichment in $\alpha\text{-MoO}_3$ significantly reduces the dephasing in the optical propagation besides the incoherence of the optical pulse itself. The propagation length L and the lifetime τ of the PhPs in isotope-enriched $\alpha\text{-MoO}_3$ have been significantly promoted to $6.76 \mu\text{m}$ and 13.9 ps at 994 cm^{-1} from $2.79 \mu\text{m}$ and 8 ps at 990

cm^{-1} , respectively. Our findings offer a new opportunity for tuning dispersion and reducing propagation loss of in-plane hyperbolic PhPs in the $\alpha\text{-MoO}_3$ at room temperature. Therefore, we envision that the isotope-enriched materials would give rise to a giant leap in polaritonic performance and facilitate polaritonic-related applications such as molecular detection, sensing, and quantum optics devices.

Methods. *Growth of the Natural $\alpha\text{-MoO}_3$ Single Crystal with Natural Distribution of Isotopes.* The $\alpha\text{-MoO}_3$ single crystal was synthesized by physical vapor deposition method using a tube furnace with open ends. The diameter of the tube furnace was 26 mm. MoO_3 powder (the natural distribution of Mo isotopes: 14.53%, ^{92}Mo ; 9.15%, ^{94}Mo ; 15.84%, ^{95}Mo ; 16.67%, ^{96}Mo ; 9.6%, ^{97}Mo ; 24.39%, ^{98}Mo ; and 9.82%, ^{100}Mo) with a purity of 99.998% (Alfa Aesar), and a weight of 0.2 g as source was placed at the center of a quartz tube. To obtain a high-quality $\alpha\text{-MoO}_3$ single crystal, the tube furnace was first heated up to 760°C in 20 min and maintained for 11 h, during which the MoO_3 powder was sublimated and recrystallized onto the low-temperature regions of the quartz tube. Second, the recrystallized $\alpha\text{-MoO}_3$ was collected and placed at the center of the tube. The tube furnace was heated up to 760°C for 20 min and maintained for 11 h again. After repeating the second step three times, the final recrystallized $\alpha\text{-MoO}_3$ crystals deposited on the low-temperature regions of the quartz tube were collected for further characterization.

Growth of Isotope-Enriched $\alpha\text{-MoO}_3$ Single Crystal. To grow isotopically pure MoO_3 crystals, we use highly pure isotope-enriched MoO_3 powder with isotope enrichment as high as $^{92}\text{Mo} = 99.9\%$ and $^{100}\text{Mo} = 99.0\%$ as source material. To grow the $\alpha\text{-}^{92}\text{MoO}_3$ single crystal, the tube was heated up to 750°C in 20 min and maintained for 9 h. To grow the $\alpha\text{-}^{100}\text{MoO}_3$ single crystal, the tube was heated up to 760°C in 20 min and held for 10 h. All heating processes are repeated four times to get high-quality $\alpha\text{-MoO}_3$ crystals.

Near-Field Optical Imaging. A commercial s-SNOM (Neaspec GmbH) is applied to perform the near-field experiment. A metallic Pt/Ir tip (Arrow-NCPt-50, Nano-World) with a 10–20 nm radius as a near-field probe could enormously enhance the light field and produce a nanoscale hot-spot. The tip operates at tapping mode with oscillation frequency at 270 kHz and oscillation amplitude at 120 nm. The tip is illuminated by a p-polarized monochromatic light from a tunable Quantum Cascade Laser (DRS Daylight Solutions), and the laser power is set to 4 mW in all near-field imaging. The pseudoheterodyne interferometric method recorded the tip-scattered light and demodulated it at the fourth harmonic of tapping frequency to suppress the dominated background signal.

■ ASSOCIATED CONTENT

SI Supporting Information

The Supporting Information is available free of charge at <https://pubs.acs.org/doi/10.1021/acs.nanolett.2c03742>.

Device fabrication and characterization, isotope enrichment of $\alpha\text{-MoO}_3$ crystals, Raman spectroscopy, infrared transmittance of $\alpha\text{-MoO}_3$ crystals, group velocities of $\alpha\text{-MoO}_3$ PhPs, lifetimes and propagation lengths in $\alpha\text{-MoO}_3$, RB_2 of the $\alpha\text{-MoO}_3$ in-plane elliptical hyperbolic PhPs, dispersion relation of the $\alpha\text{-MoO}_3$ (PDF)

■ AUTHOR INFORMATION

Corresponding Authors

Lihong Bao — Beijing National Laboratory for Condensed Matter Physics, Institute of Physics, Chinese Academy of Sciences, Beijing 100190, China; School of Physical Sciences, University of Chinese Academy of Sciences, Beijing 100049, China; Songshan Lake Materials Laboratory, Dongguan, Guangdong 523808, China;  orcid.org/0000-0002-2942-892X; Email: lhbao@iphy.ac.cn

Jianing Chen — Beijing National Laboratory for Condensed Matter Physics, Institute of Physics, Chinese Academy of Sciences, Beijing 100190, China; School of Physical Sciences, University of Chinese Academy of Sciences, Beijing 100049, China; Songshan Lake Materials Laboratory, Dongguan, Guangdong 523808, China; Email: jnchen@iphy.ac.cn

Authors

Yongqian Zhao — Beijing National Laboratory for Condensed Matter Physics, Institute of Physics, Chinese Academy of Sciences, Beijing 100190, China; School of Physical Sciences, University of Chinese Academy of Sciences, Beijing 100049, China;  orcid.org/0000-0002-1828-5476

Jiancui Chen — Beijing National Laboratory for Condensed Matter Physics, Institute of Physics, Chinese Academy of Sciences, Beijing 100190, China; School of Physical Sciences, University of Chinese Academy of Sciences, Beijing 100049, China

Mengfei Xue — Wenzhou Institute, University of Chinese Academy of Sciences, Wenzhou 325001, China; School of Physical Sciences, University of Chinese Academy of Sciences, Beijing 100049, China; Beijing National Laboratory for Condensed Matter Physics, Institute of Physics, Chinese Academy of Sciences, Beijing 100190, China;  orcid.org/0000-0001-5037-5925

Runkun Chen — Beijing National Laboratory for Condensed Matter Physics, Institute of Physics, Chinese Academy of Sciences, Beijing 100190, China; School of Physical Sciences, University of Chinese Academy of Sciences, Beijing 100049, China;  orcid.org/0000-0003-3410-4863

Shangtong Jia — State Key Laboratory for Mesoscopic Physics, School of Physics, Peking University, Beijing 100871, China

Jianjun Chen — Department of Physics and Applied Optics Beijing Area Major Laboratory, Beijing Normal University, Beijing 100875, China; State Key Laboratory for Mesoscopic Physics, School of Physics, Peking University, Beijing 100871, China; Collaborative Innovation Center of Extreme Optics, Shanxi University, Taiyuan, Shanxi 030006, China

Hong-Jun Gao — Beijing National Laboratory for Condensed Matter Physics, Institute of Physics, Chinese Academy of Sciences, Beijing 100190, China; School of Physical Sciences, University of Chinese Academy of Sciences, Beijing 100049, China; Songshan Lake Materials Laboratory, Dongguan, Guangdong 523808, China;  orcid.org/0000-0002-6766-0623

Complete contact information is available at:

<https://pubs.acs.org/10.1021/acs.nanolett.2c03742>

Author Contributions

J.N.C. conceived the idea and supervised the work. J.C.C. synthesized all α -MoO₃ crystals under the direction of L.H.B. and H.J.G. Y.Q.Z. prepared the samples and conducted Raman, XRD, and s-SNOM measurements. J.N.C., Y.Q.Z., and M.F.X. analyzed and interpreted the results. R.K.C. helped

with the calculation of the dispersion relation of α -MoO₃. S.T.J. helped with the fabrication of the α -MoO₃ disks under the direction of J.J.C. Y.Q.Z. and J.N.C. wrote the manuscript. All authors contributed to the final version of the manuscript.

Notes

The authors declare no competing financial interest.

■ ACKNOWLEDGMENTS

We acknowledge research supports from the National Key Research and Development Program of China (Grant Nos. 2016YFA0203500, 2016YFA0202300, and 2018YFA0704401), National Natural Science Foundation of China (Grant Nos. 11874407, 61888102, 61922002, 12204125, and 91850103), Strategic Priority Research Program of Chinese Academy of Sciences (Grant No. XDB 30000000), Youth Innovation Promotion Association of C.A.S. (Y201902), Beijing Natural Science Foundation (Z180015), and China Postdoctoral Science Foundation (Grant No. 2021M703173).

■ REFERENCES

- (1) Basov, D. N.; Fogler, M. M.; García De Abajo, F. J. Polaritons in van der Waals materials. *Science* **2016**, *354*, aag1992.
- (2) Low, T.; Chaves, A.; Caldwell, J. D.; Kumar, A.; Fang, N. X.; Avouris, P.; Heinz, T. F.; Guinea, F.; Martin-Moreno, L.; Koppens, F. Polaritons in layered two-dimensional materials. *Nat. Mater.* **2017**, *16*, 182–194.
- (3) Chen, J.; Badioli, M.; Alonso-González, P.; Thongrattanasiri, S.; Huth, F.; Osmond, J.; Spasenović, M.; Centeno, A.; Pesquera, A.; Godignon, P.; Zurutuza Elorza, A.; Camara, N.; de Abajo, F. J. G.; Hillenbrand, R.; Koppens, F. H. L. Optical nano-imaging of gate-tunable graphene plasmons. *Nature* **2012**, *487*, 77–81.
- (4) Fei, Z.; Rodin, A. S.; Andreev, G. O.; Bao, W.; McLeod, A. S.; Wagner, M.; Zhang, L. M.; Zhao, Z.; Thiemens, M.; Dominguez, G.; Fogler, M. M.; Neto, A. H. C.; Lau, C. N.; Keilmann, F.; Basov, D. N. Gate-tuning of graphene plasmons revealed by infrared nano-imaging. *Nature* **2012**, *487*, 82–85.
- (5) Ni, G. X.; Wang, H.; Wu, J. S.; Fei, Z.; Goldflam, M. D.; Keilmann, F.; Özyilmaz, B.; Castro Neto, A. H.; Xie, X. M.; Fogler, M. M.; Basov, D. N. Plasmons in graphene moiré superlattices. *Nat. Mater.* **2015**, *14*, 1217–1222.
- (6) Ni, G. X.; Wang, L.; Goldflam, M. D.; Wagner, M.; Fei, Z.; McLeod, A. S.; Liu, M. K.; Keilmann, F.; Özyilmaz, B.; Castro Neto, A. H.; Hone, J.; Fogler, M. M.; Basov, D. N. Ultrafast optical switching of infrared plasmon polaritons in high-mobility graphene. *Nat. Photonics* **2016**, *10*, 244–247.
- (7) Lu, Y.-J.; Kim, J.; Chen, H.-Y.; Wu, C.; Dabidian, N.; Sanders, C. E.; Wang, C.-Y.; Lu, M.-Y.; Li, B.-H.; Qiu, X.; et al. Plasmonic nanolaser using epitaxially grown silver film. *Science* **2012**, *337*, 450–453.
- (8) Wei, H.; Zhang, S.; Tian, X.; Xu, H. Highly tunable propagating surface plasmons on supported silver nanowires. *Proc. Natl. Acad. Sci. U.S.A.* **2013**, *110*, 4494–4499.
- (9) Hu, D.; Yang, X.; Li, C.; Liu, R.; Yao, Z.; Hu, H.; Corder, S. N. G.; Chen, J.; Sun, Z.; Liu, M.; Dai, Q. Probing optical anisotropy of nanometer-thin van der waals microcrystals by near-field imaging. *Nat. Commun.* **2017**, *8*, 1471.
- (10) Hu, F.; Luan, Y.; Scott, M. E.; Yan, J.; Mandrus, D. G.; Xu, X.; Fei, Z. Imaging exciton–polariton transport in MoSe₂ waveguides. *Nat. Photonics* **2017**, *11*, 356–360.
- (11) Mrejen, M.; Yadgarov, L.; Levanon, A.; Suchowski, H. Transient exciton-polariton dynamics in WSe₂ by ultrafast near-field imaging. *Sci. Adv.* **2019**, *5*, eaat9618.
- (12) Chen, Y.-J.; Cain, J. D.; Stanev, T. K.; Dravid, V. P.; Stern, N. P. Valley-polarized exciton–polaritons in a monolayer semiconductor. *Nat. Photonics* **2017**, *11*, 431–435.
- (13) Li, P.; Dolado, I.; Alfaro-Mozaz, F. J.; Casanova, F.; Hueso, L. E.; Liu, S.; Edgar, J. H.; Nikitin, A. Y.; Vélez, S.; Hillenbrand, R.

- Infrared hyperbolic metasurface based on nanostructured van der Waals materials. *Science* **2018**, *359*, 892–896.
- (14) Chaudhary, K.; Tamagnone, M.; Rezaee, M.; Bediako, D. K.; Ambrosio, A.; Kim, P.; Capasso, F. Engineering phonon polaritons in van der Waals heterostructures to enhance in-plane optical anisotropy. *Sci. Adv.* **2019**, *5*, eaau7171.
- (15) Hu, G.; Ou, Q.; Si, G.; Wu, Y.; Wu, J.; Dai, Z.; Krasnok, A.; Mazor, Y.; Zhang, Q.; Bao, Q.; Qiu, C.-W.; Alù, A. Topological polaritons and photonic magic angles in twisted α -MoO₃ bilayers. *Nature* **2020**, *582*, 209–213.
- (16) Duan, J.; Capote-Robayna, N.; Taboada-Gutiérrez, J.; Álvarez-Pérez, G.; Prieto, I.; Martín-Sánchez, J.; Nikitin, A. Y.; Alonso-González, P. Twisted Nano-Optics: Manipulating Light at the Nanoscale with Twisted Phonon Polaritonic Slabs. *Nano Lett.* **2020**, *20*, 5323–5329.
- (17) Dai, S.; Fei, Z.; Ma, Q.; Rodin, A.; Wagner, M.; McLeod, A.; Liu, M.; Gannett, W.; Regan, W.; Watanabe, K.; et al. Tunable phonon polaritons in atomically thin van der Waals crystals of boron nitride. *Science* **2014**, *343*, 1125–1129.
- (18) Duan, J.; Chen, R.; Li, J.; Jin, K.; Sun, Z.; Chen, J. Launching Phonon Polaritons by Natural Boron Nitride Wrinkles with Modifiable Dispersion by Dielectric Environments. *Adv. Mater.* **2017**, *29*, 1702494.
- (19) Alfaro-Mozaz, F. J.; Alonso-González, P.; Vélez, S.; Dolado, I.; Autore, M.; Mastel, S.; Casanova, F.; Hueso, L. E.; Li, P.; Nikitin, A. Y.; Hillenbrand, R. Nanoimaging of resonating hyperbolic polaritons in linear boron nitride antennas. *Nat. Commun.* **2017**, *8*, 15624.
- (20) Bylinkin, A.; Schnell, M.; Autore, M.; Calavalle, F.; Li, P.; Taboada-Gutiérrez, J.; Liu, S.; Edgar, J. H.; Casanova, F.; Hueso, L. E.; Alonso-Gonzalez, P.; Nikitin, A. Y.; Hillenbrand, R. Real-space observation of vibrational strong coupling between propagating phonon polaritons and organic molecules. *Nat. Photonics* **2021**, *15*, 197–202.
- (21) Li, P.; Lewin, M.; Kretinin, A. V.; Caldwell, J. D.; Novoselov, K. S.; Taniguchi, T.; Watanabe, K.; Gaussmann, F.; Taubner, T. Hyperbolic phonon-polaritons in boron nitride for near-field optical imaging and focusing. *Nat. Commun.* **2015**, *6*, 7507.
- (22) Li, P.; Dolado, I.; Alfaro-Mozaz, F. J.; Nikitin, A. Y.; Casanova, F.; Hueso, L. E.; Vélez, S.; Hillenbrand, R. Optical Nanoimaging of Hyperbolic Surface Polaritons at the Edges of van der Waals Materials. *Nano Lett.* **2017**, *17*, 228–235.
- (23) Dai, S.; Tymchenko, M.; Yang, Y.; Ma, Q.; Pita-Vidal, M.; Watanabe, K.; Taniguchi, T.; Jarillo-Herrero, P.; Fogler, M. M.; Alù, A.; Basov, D. N. Manipulation and Steering of Hyperbolic Surface Polaritons in Hexagonal Boron Nitride. *Adv. Mater.* **2018**, *30*, 1706358.
- (24) Dai, S.; Ma, Q.; Andersen, T.; McLeod, A. S.; Fei, Z.; Liu, M. K.; Wagner, M.; Watanabe, K.; Taniguchi, T.; Thiemens, M.; Keilmann, F.; Jarillo-Herrero, P.; Fogler, M. M.; Basov, D. N. Subdiffractive focusing and guiding of polaritonic rays in a natural hyperbolic material. *Nat. Commun.* **2015**, *6*, 6963.
- (25) Ma, W.; Alonso-González, P.; Li, S.; Nikitin, A. Y.; Yuan, J.; Martín-Sánchez, J.; Taboada-Gutiérrez, J.; Amenabar, I.; Li, P.; Vélez, S.; Tollar, C.; Dai, Z.; Zhang, Y.; Sriram, S.; Kalantar-Zadeh, K.; Lee, S.-T.; Hillenbrand, R.; Bao, Q. In-plane anisotropic and ultra-low-loss polaritons in a natural van der Waals crystal. *Nature* **2018**, *562*, 557–562.
- (26) Zheng, Z.; Chen, J.; Wang, Y.; Wang, X.; Chen, X.; Liu, P.; Xu, J.; Xie, W.; Chen, H.; Deng, S.; Xu, N. Highly Confined and Tunable Hyperbolic Phonon Polaritons in Van Der Waals Semiconducting Transition Metal Oxides. *Adv. Mater.* **2018**, *30*, 1705318.
- (27) Taboada-Gutiérrez, J.; Álvarez-Pérez, G.; Duan, J.; Ma, W.; Crowley, K.; Prieto, I.; Bylinkin, A.; Autore, M.; Volkova, H.; Kimura, K.; Kimura, T.; Berger, M. H.; Li, S.; Bao, Q.; Gao, X. P. A.; Errea, I.; Nikitin, A. Y.; Hillenbrand, R.; Martín-Sánchez, J.; Alonso-González, P. Broad spectral tuning of ultra-low-loss polaritons in a van der Waals crystal by intercalation. *Nat. Mater.* **2020**, *19*, 964–968.
- (28) Dai, S.; Ma, Q.; Liu, M. K.; Andersen, T.; Fei, Z.; Goldflam, M. D.; Wagner, M.; Watanabe, K.; Taniguchi, T.; Thiemens, M.; Keilmann, F.; Jarillo-Herrero, P.; Fogler, M. M.; Basov, D. N. Efficiency of Launching Highly Confined Polaritons by Infrared Light Incident on a Hyperbolic Material. *Nano Lett.* **2017**, *17*, 5285–5290.
- (29) Fali, A.; White, S. T.; Folland, T. G.; He, M.; Aghamiri, N. A.; Liu, S.; Edgar, J. H.; Caldwell, J. D.; Haglund, R. F.; Abate, Y. Refractive Index-Based Control of Hyperbolic Phonon-Polariton Propagation. *Nano Lett.* **2019**, *19*, 7725–7734.
- (30) Schwartz, J. J.; Le, S. T.; Krylyuk, S.; Richter, C. A.; Davydov, A. V.; Centrone, A. Substrate-mediated hyperbolic phonon polaritons in MoO₃. *Nanophotonics* **2021**, *10*, 1517–1527.
- (31) Ni, G. X.; McLeod, A. S.; Sun, Z.; Wang, L.; Xiong, L.; Post, K. W.; Sunku, S. S.; Jiang, B. Y.; Hone, J.; Dean, C. R.; Fogler, M. M.; Basov, D. N. Fundamental limits to graphene plasmonics. *Nature* **2018**, *557*, 530–533.
- (32) Giles, A. J.; Dai, S.; Vurgaftman, I.; Hoffman, T.; Liu, S.; Lindsay, L.; Ellis, C. T.; Assefa, N.; Chatzakis, I.; Reinecke, T. L.; Tischler, J. G.; Fogler, M. M.; Edgar, J. H.; Basov, D. N.; Caldwell, J. D. Ultralow-loss polaritons in isotopically pure boron nitride. *Nat. Mater.* **2018**, *17*, 134–139.
- (33) Wang, L.; Chen, R.; Xue, M.; Liu, S.; Edgar, J. H.; Chen, J. Manipulating phonon polaritons in low loss ¹¹B enriched hexagonal boron nitride with polarization control. *Nanoscale* **2020**, *12*, 8188–8193.
- (34) Ni, G.; McLeod, A. S.; Sun, Z.; Matson, J. R.; Lo, C. F. B.; Rhodes, D. A.; Ruta, F. L.; Moore, S. L.; Vitalone, R. A.; Cusco, R.; Artús, L.; Xiong, L.; Dean, C. R.; Hone, J. C.; Millis, A. J.; Fogler, M. M.; Edgar, J. H.; Caldwell, J. D.; Basov, D. N. Long-Lived Phonon Polaritons in Hyperbolic Materials. *Nano Lett.* **2021**, *21*, 5767–5773.
- (35) Chen, K.; Song, B.; Ravichandran, N. K.; Zheng, Q.; Chen, X.; Lee, H.; Sun, H.; Li, S.; Gamage, G. A. G. U.; Tian, F.; et al. Ultrahigh thermal conductivity in isotope-enriched cubic boron nitride. *Science* **2020**, *367*, 555–559.
- (36) Zheng, Q.; Li, S.; Li, C.; Lv, Y.; Liu, X.; Huang, P. Y.; Broido, D. A.; Lv, B.; Cahill, D. G. High Thermal Conductivity in Isotopically Enriched Cubic Boron Phosphide. *Adv. Funct. Mater.* **2018**, *28*, 1805116.
- (37) Cai, Q.; Scullion, D.; Gan, W.; Falin, A.; Cizek, P.; Liu, S.; Edgar, J. H.; Liu, R.; Cowie, B. C. C.; Santos, E. J. G.; Li, L. H. Outstanding Thermal Conductivity of Single Atomic Layer Isotope-Modified Boron Nitride. *Phys. Rev. Lett.* **2020**, *125*, No. 085902.
- (38) Zheng, Z.; Xu, N.; Oscurato, S. L.; Tamagnone, M.; Sun, F.; Jiang, Y.; Ke, Y.; Chen, J.; Huang, W.; Wilson, W. L.; et al. A mid-infrared biaxial hyperbolic van der Waals crystal. *Sci. Adv.* **2019**, *5*, eaav8690.
- (39) Duan, J.; Álvarez-Pérez, G.; Voronin, K. V.; Prieto, I.; Taboada-Gutiérrez, J.; Volkov, V. S.; Martín-Sánchez, J.; Nikitin, A. Y.; Alonso-González, P. Enabling propagation of anisotropic polaritons along forbidden directions via a topological transition. *Sci. Adv.* **2021**, *7*, eabf2690.
- (40) Dai, Z.; Hu, G.; Si, G.; Ou, Q.; Zhang, Q.; Balendhran, S.; Rahman, F.; Zhang, B. Y.; Ou, J. Z.; Li, G.; Alù, A.; Qiu, C.-W.; Bao, Q. Edge-oriented and steerable hyperbolic polaritons in anisotropic van der Waals nanocavities. *Nat. Commun.* **2020**, *11*, 6086.
- (41) Wen, M.; Chen, X.; Zheng, Z.; Deng, S.; Li, Z.; Wang, W.; Chen, H. In-Plane Anisotropic Raman Spectroscopy of van der Waals α -MoO₃. *J. Phys. Chem. C* **2021**, *125*, 765–773.
- (42) Woessner, A.; Lundeberg, M. B.; Gao, Y.; Principi, A.; Alonso-González, P.; Carrega, M.; Watanabe, K.; Taniguchi, T.; Vignale, G.; Polini, M.; Hone, J.; Hillenbrand, R.; Koppens, F. H. L. Highly confined low-loss plasmons in graphene–boron nitride heterostructures. *Nat. Mater.* **2015**, *14*, 421–425.
- (43) Dai, S.; Ma, Q.; Yang, Y.; Rosenfeld, J.; Goldflam, M. D.; McLeod, A.; Sun, Z.; Andersen, T. I.; Fei, Z.; Liu, M.; Shao, Y.; Watanabe, K.; Taniguchi, T.; Thiemens, M.; Keilmann, F.; Jarillo-Herrero, P.; Fogler, M. M.; Basov, D. N. Efficiency of Launching Highly Confined Polaritons by Infrared Light Incident on a Hyperbolic Material. *Nano Lett.* **2017**, *17*, 5285–5290.

- (44) Wong, K. P.; Hu, X.; Lo, T. W.; Guo, X.; Fung, K. H.; Zhu, Y.; Lau, S. P. Edge-Orientation Dependent Nanoimaging of Mid-Infrared Waveguide Modes in High-Index PtSe₂. *Adv. Opt. Mater.* **2021**, *9*, 2100294.
- (45) Barik, A.; Otto, L. M.; Yoo, D.; Jose, J.; Johnson, T. W.; Oh, S.-H. Dielectrophoresis-Enhanced Plasmonic Sensing with Gold Nano-hole Arrays. *Nano Lett.* **2014**, *14*, 2006–2012.
- (46) Xomalis, A.; Zheng, X.; Demetriadou, A.; Martínez, A.; Chikkaraddy, R.; Baumberg, J. J. Interfering Plasmons in Coupled Nanoresonators to Boost Light Localization and SERS. *Nano Lett.* **2021**, *21*, 2512–2518.

□ Recommended by ACS

The Dissociation of Exciton During the Lasing of a Single CsPbBr₃ Microplate

Xiuru Yao, Yongjun Bao, *et al.*

NOVEMBER 16, 2022

THE JOURNAL OF PHYSICAL CHEMISTRY LETTERS

READ ▾

Phosphites: A Nonlinear Optical Materials System with a Wide Band Gap and Moderate Second-Harmonic Generation Effect

Jingjing Zhang, Bingbing Zhang, *et al.*

NOVEMBER 08, 2022

INORGANIC CHEMISTRY

READ ▾

Enhanced Second-Harmonic Generation of van der Waals CuInP₂S₆ via Pressure-Regulated Cationic Displacement

Kejun Bu, Xujie Lü, *et al.*

DECEMBER 16, 2022

CHEMISTRY OF MATERIALS

READ ▾

Anisotropic Infrared Response and Orientation-Dependent Strain-Tuning of the Electronic Structure in Nb₂SiTe₄

Fanjie Wang, Hugen Yan, *et al.*

APRIL 26, 2022

ACS NANO

READ ▾

[Get More Suggestions >](#)